

## Xuan Liang

Department of Mechanical Engineering,  
Carnegie Mellon University,  
Pittsburgh, PA 15213  
e-mail: xliang3@andrew.cmu.edu

## Lisha White

Department of Mechanical Engineering,  
Carnegie Mellon University,  
Pittsburgh, PA 15213  
e-mail: lnwhite@andrew.cmu.edu

## Jonathan Cagan

Fellow ASME  
Professor  
Department of Mechanical Engineering,  
Carnegie Mellon University,  
Pittsburgh, PA 15213  
e-mail: cagan@cmu.edu

## Anthony D. Rollett

Professor  
Department of Materials Science and Engineering,  
Carnegie Mellon University,  
Pittsburgh, PA 15213  
e-mail: rollett@andrew.cmu.edu

## Yongjie Jessica Zhang<sup>1</sup>

Fellow ASME  
Professor  
Department of Mechanical Engineering,  
Carnegie Mellon University,  
Pittsburgh, PA 15213  
e-mail: jessicaz@andrew.cmu.edu

# Unit-Based Design of Cross-Flow Heat Exchangers for LPBF Additive Manufacturing

*The structural design and additive manufacturing (AM) of cross-flow heat exchangers (HXs) are studied. A unit-based design framework is proposed to optimize the channel configuration in order to improve the heat exchange performance (HXP) and meanwhile control the pressure drop (PD) between the fluid inlet and outlet. A gradient-based optimization methodology is employed to drive the design process. Both shape and topology changes are observed during the channel configuration evolution. Moreover, AM printability evaluation is considered and some re-design work is proposed to improve the printability of the designs with respect to the metal laser powder bed fusion (LPBF) process. For an optimized structure from the unit-based design, corner rounding operation is adopted first, specifically to avoid sharp features. Then the building process of the entire HX containing top, bottom caps, side walls, and the optimized thin-walled channels is simulated, and residual deformation is predicted through sequential layer-by-layer analysis. Based on the residual deformation profile, geometrical compensation is implemented to reduce geometrical inaccuracy of the printed HX. In addition, build orientation selection is also studied to avoid overhang issues in some specific unit-based design results. Finally, a mature design scheme for the cross-flow HX can be achieved as the solution that leads to largely improved HXP (e.g., nearly 200% increase), well controlled PD, and enhanced printability with respect to the LPBF AM process. [DOI: 10.1115/1.4055734]*

**Keywords:** cross-flow heat exchanger, unit-based design, printability evaluation, laser powder bed fusion, design for manufacturing, multidisciplinary design and optimization, simulation-based design, topology optimization

## 1 Introduction

Heat exchangers (HXs) have been widely used in the industrial equipment and devices, such as vehicles, chemical reactors, and electronic machines. Among various HXs, the two-fluid HX is the most popular type. Moreover, according to the flow directions, two-fluid HXs can be further classified into three categories: cross-flow, counter-current, and co-current HXs. The heat exchange performance (HXP) and the pressure drop (PD) are two most important indices to evaluate the performance of the HXs. Naturally, many efforts have been devoted to the design of HXs for the purpose of improving the HXP while controlling the PD. Specifically, shape and topology optimization have been the most popular and successful methodology for HX design thus far [1,2].

The thin-walled channel structures are commonly seen in the HXs, especially two-fluid shell-tube HXs [3]. These channels separate two different fluids at different temperatures and maintain good heat transfer. Usually, complex channel configurations are employed to enhance the heat exchanging process in the HXs, which may cause difficulty in manufacturing these thin-walled channels using the conventional production process. Additive manufacturing (AM) has the inherent advantage in building complex

components in a bottom-up, net-shaping fashion. Therefore, it has been widely employed in the production of HXs, especially considering some novel designs with very complex internal structures [4]. There still exists some challenges with manufacturing the HXs with AM. Due to the rapid phase change from powder to liquid to solid, an excess of residual stress can accumulate. These residuals also yield large residual deformation in the finished metal components, causing severe geometrical errors compared to the desired geometry, making the printed components a waste of time and material [5]. Moreover, large residual deformation may result in build failure in the bottom-up layer-wise printing process [6]. These challenges highlight the importance of considering residual deformation as a parameter to determine the printability of a component. If large residual deformation is predicted for a given component, it indicates weak printability and the component should not be put into the practical AM process.

In the recent years, there have been advances within the structural design field that incorporate designs for AM [7–9]. For example, a self-support constraint was incorporated in some topology optimization researches aimed at compliance minimization to avoid overhang issue in the optimized structures [10]. To handle material connection issues, an additive manufactured thin-walled lattice structure was used to reconstruct the optimized structure in structural-acoustic topology optimization [11]. In addition, several recent works presented optimization methodologies specifically for support structure design with an objective of residual deformation mitigation for the supported depositions [12]. Nonetheless, only some simple builds were studied, such as a cantilever beam. This is in part attributed to the computationally expensive

<sup>1</sup>A short version was submitted to the ASME IDETC-DAC 2022 as a technical paper.

<sup>1</sup>Corresponding author.

Contributed by the Design Automation Committee of ASME for publication in the JOURNAL OF MECHANICAL DESIGN. Manuscript received February 23, 2022; final manuscript received September 7, 2022; published online October 10, 2022. Assoc. Editor: Deepesh Toshniwal.

evaluation of residual deformation for complex AM components. There also exists a lack of research on the design study of HXs that improves the HXP while considering AM printability of the optimized structures. Despite the benefits laser powder bed fusion (LPBF) offers (e.g., manufacturing complex metal shapes at high-quality and in nearly net-shaping fashion), manufacturing is impractical without application of design for AM rules. To this end, the motivation of this study is to propose a framework to design the optimized HXs manufacturable with LPBF AM.

The remainder of the paper is organized as follows. First, Sec. 2 discusses the problem description and framework overview. Multiphysics governing equations are introduced for the two-fluid cross-flow HX. Moreover, the residual deformation issue in the AM process for the thin-walled HX is also explained. Then the mathematical model for HX shape/topology optimization is explained in Sec. 3. In Sec. 4, residual deformation simulation is presented in detail for the HX containing thin-walled channel structures. Numerical results on unit-based design and re-design work for AM printability improvement as well as some discussions are presented in Sec. 5. Finally, the conclusions and future work are given in Sec. 6.

## 2 Problem Description and Framework Overview

In this section, the involved problems are described first, including the fluid-thermal multiphysics problem and residual deformation-related AM printability issue. For which, the governing equations are given accordingly. Then the framework overview of this paper is presented.

**2.1 Fluid-Thermal Problem for Heat Exchanger.** The two-fluid cross-flow HX is considered in this study. The cold and hot fluids flow into the internal space of the heat exchanger in two perpendicular directions and are separated by thin-walled channels as shown in Fig. 1 (left panel). This configuration can be simplified as a 2D problem by looking at a cutting plane and neglecting the wall thickness of the vertical channels in the cross-flow HX as shown in Fig. 1 (right panel).

The incompressible steady-state Navier–Stokes equations are taken as the governing equation for the fluid velocity and pressure fields. We have

$$\begin{cases} \operatorname{div}(\rho \mathbf{u} \otimes \mathbf{u}) + \nabla p - \nu \Delta \mathbf{u} = \mathbf{F} & \text{in } \Omega_f \\ \operatorname{div}(\mathbf{u}) = 0 & \text{in } \Omega_f \\ \mathbf{u} = \mathbf{u}_0 & \text{at fluid inlet} \\ \mathbf{u} = 0 & \text{at wall} \end{cases} \quad (1)$$

where  $\mathbf{u}$  and  $p$  are the velocity and pressure fields, respectively.  $\rho$  is the fluid mass density,  $\nu$  is the fluid dynamic viscosity,  $\Omega_f$  is the fluid domain, and  $\mathbf{F}$  denotes body force for the two-fluid system. For simplification, zero body force is considered in this paper. Regarding the boundary conditions, non-slip constraint is applied to the upper and lower boundaries of the design domain. A parabolic distribution is adopted to define the velocity boundary

condition for the cold fluid inlet. In addition, to avoid expensive computational cost caused by dynamic remeshing when the interface between two fluids changes, a non-body-fitted mesh is employed for the design domain in this work. Accordingly, specific boundary condition like zero velocity is applied to those regions representing the hot fluid.

The steady-state heat convection–diffusion equation is taken as the governing equation for the fluid temperature field. It is written as

$$\begin{cases} -\operatorname{div}(k_f \nabla T) + \rho c_p \mathbf{u} \cdot \nabla T = 0 & \text{in } \Omega_f \\ \frac{\partial T}{\partial \mathbf{n}} = 0 & \text{at wall} \\ T = T_{\text{in}} & \text{at fluid inlet} \end{cases} \quad (2)$$

where  $k_f$  is the thermal conductivity coefficient, and  $c_p$  is the thermal capacity coefficient.  $\mathbf{n}$  is the surface normal vector for the specific boundary. Given the non-body-fitted mesh for the design domain, fixed high temperature is enforced to the hot fluid region as a specific boundary condition. Note fluid velocity field  $\mathbf{u}$  is coupled in Eq. (2). For the numerical implementation, the Navier–Stokes equations are first solved to obtain the velocity field. This field is then taken as an input in solving the heat convection–diffusion equation.

For the steady-state Navier–Stokes equations and the heat convection–diffusion equation, the Reynolds number (Re) and the Peclet number (Pe) are defined as

$$\operatorname{Re} = \frac{\rho \mathbf{u}_{\text{in}} L}{\nu}, \quad \operatorname{Pe} = \frac{\rho c_p \mathbf{u}_{\text{in}} L}{k_f} \quad (3)$$

where  $\mathbf{u}_{\text{in}}$  denotes the fluid velocity magnitude infinitely far away from the inlet, and  $L$  denotes the characteristic length of the HX. In this paper, the width is selected as the characteristic length. The fluid density,  $\rho$ , and the heat capacity coefficient,  $c_p$ , take unit values to simplify the computation of Re and Pe values. Since the characteristic length  $L$  is constant, only the fluid dynamic viscosity,  $\nu$ , and the thermal conductivity coefficient,  $k_f$ , are parameterized to achieve different Re and Pe values.

**2.2 Additive Manufacturing Printability—Residual Deformation.** LPBF is an AM technology that uses a laser to melt powder material in a layer-wise fashion to build a part. It is a commonly used process to repeatedly create low-volume, complex metal components at various scales. Since LPBF is a desirable manufacturing process for the complex HX geometry, careful consideration must be given to the printability of near-net shape structures. Given a cross-flow HX, the intended build direction is to print the thin-walled channels vertically. In this work, residual deformation incurring in the bottom-up layer-by-layer printing process is simulated by the modified inherent strain (MIS) method [13,14]. The governing equation for this sequential analysis is written as

$$\begin{cases} \nabla \cdot \boldsymbol{\sigma}_i = 0 \\ \boldsymbol{\sigma}_i = \mathbf{E} \boldsymbol{\varepsilon}_e^i \\ \boldsymbol{\varepsilon}_{\text{tot}}^i = \boldsymbol{\varepsilon}_e^i + \boldsymbol{\varepsilon}_p^i + \boldsymbol{\varepsilon}_{\text{in}}^i \end{cases} \quad (4)$$

where  $\boldsymbol{\sigma}_i$  denotes the stress field when the  $i$ th layer is printed and  $\mathbf{E}$  is the constitutive elasticity tensor. The remaining symbols  $\boldsymbol{\varepsilon}_e^i$ ,  $\boldsymbol{\varepsilon}_p^i$ ,  $\boldsymbol{\varepsilon}_{\text{in}}^i$ , and  $\boldsymbol{\varepsilon}_{\text{tot}}^i$  denote the elastic, plastic, inherent, and total strain field for the  $i$ th step, respectively. As a clarification, since the contribution of thermal strain to the residual stress and deformation is considered in the formulation of the inherent strain, it is not included in Eq. (4). The solution in the current step is taken as the initial condition for the following step in the layer-wise simulation until the entire HX is printed.

**2.3 Additive Manufacturing-Oriented Heat Exchanger Design.** The design problem we aim to address is the incorporation of AM rules into the shape and topology optimization of HXs for LPBF. These design rules have been extensively studied and validated but only a few have yet to be applied for HX design. For

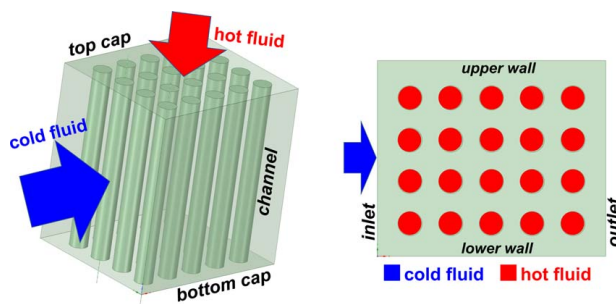


**Fig. 1** Profile of 3D cross-flow heat exchanger and a simplified 2D view. The cold and hot fluids flow in two perpendicular directions and are separated from mixing by the thin-walled channels.

example, the rules provide guidelines on how to mitigate the effects of thin features which cause unwanted fusion between independent feature boundaries [15]. Thus, we perform shape/topology optimization to improve the HXP and control the PD of the cross-flow HX, while improving its printability with respect to the LPBF AM process. The multiphysics governing equations in Sec. 2.1 are solved to compute the HXP and PD values of the HX as well as derivatives of the design variables. We employ a mathematical optimization algorithm to change shape and topology of the HX, searching for the optimal configuration with maximized HXP while limiting its PD.

To implement the design for AM rules, the structural design result is examined considering practical manufacturability requirements of the LPBF process to ensure the printability of high-quality HXs. The re-design problem will be considered to eliminate some problematic issues, making the numerical design result suitable for the LPBF process. For example, unwanted features such as sharp corners should be avoided. In particular, residual deformation of the 3D reconstructed optimized structure will be simulated by solving the governing equation in Sec. 2.2. This simulation will be used to check its after-printing geometrical accuracy. The original optimized configuration will be re-designed if large residual deformation is observed. Moreover, the overhang issue from the optimized structure will also be considered in the re-design problem. The needs for the above AM printability considerations are justified by references to Ref. [16] in this paper, and in future work we will print test articles for further exploration.

**2.4 Design Framework Overview.** This section proposes a novel framework to design HXs ready for LPBF AM, summarized in Fig. 2. The framework consists of two functional procedures: the unit-based design and printability evaluation processes. In this study, a unit-based design is chosen in contrast to domain-based design. The latter denotes regular shape/topology optimization where design variables are defined in the entire design domain, while the former denotes the specific case where design variables are defined based on the sub-domain dividing the design space. In choosing the unit-based design approach, the number of design variables can be greatly reduced. The unit-based design may also provide particular benefit with respect to AM fabrication of cross-flow HX. This point will be elucidated in detail in Sec. 5. The isogeometric analysis (IGA) [17–19] and the optimization modules are contained in the unit-based design process. IGA is employed to solve the steady-state Navier–Stokes and convection–diffusion equations to evaluate the HXP and the PD. Then, a gradient-based

optimization methodology is adopted to search for the optimized HX design.

In the printability evaluation process, the unit-based design result is examined in accordance to the practical AM process. Due to simplifications made to reduce the model to 2D, some re-design work is applied to the unit-based design result with three techniques. The purpose is to improve the printability of the numerical designs obtained from the first process. This re-design process is not coupled into the unit-based design process due to expensive computational cost. First, corner rounding operation is employed to remove sharp protrusions in the channel shape. Then the processed structure is taken as input for residual deformation simulation. The governing equation for MIS-based sequential analysis is solved by finite element analysis. Based on the MIS-based simulation, geometrical compensation is employed to reduce geometrical inaccuracy of the final build. Lastly, build orientation re-design is also considered for some specific optimized structures. As the output of the entire framework, we expect to obtain a finalized design for the cross-flow HX with improved performance and AM printability.

### 3 Mathematical Model for Heat Exchanger Design

The formulations for design optimization of the 2D cross-flow HX are introduced briefly in this section. We first define the objective and constraint functions for our mathematical model. This study focuses on the HXP improvement and the PD control when considering the design of HXs. Thus, the HXP is taken as the objective function, while the PD is considered as the constraint for our optimization model. The explicit expressions of the HXP and the PD are given based on the fluid velocity and pressure fields as

$$\text{HXP} = \int_{\Omega_f} \rho c_p \mathbf{u} \cdot \nabla T d\Omega \quad (5)$$

$$\text{PD} = \left( \int_{\partial\Omega_{f,i}} p dS - \int_{\partial\Omega_{f,o}} p dS \right) / A \quad (6)$$

where  $\partial\Omega_{f,i}$  and  $\partial\Omega_{f,o}$  denote the boundary surface of the fluid inlet and outlet, respectively.  $A$  denotes the area of the fluid inlet/outlet. For simplicity, the involved parameters such as  $\rho$  and  $c_p$  take unit values when solving the governing equations and calculating the HXP and the PD. Zero velocity is assumed for the hot fluid in the channels in this paper. Given this assumption, the flow resistance

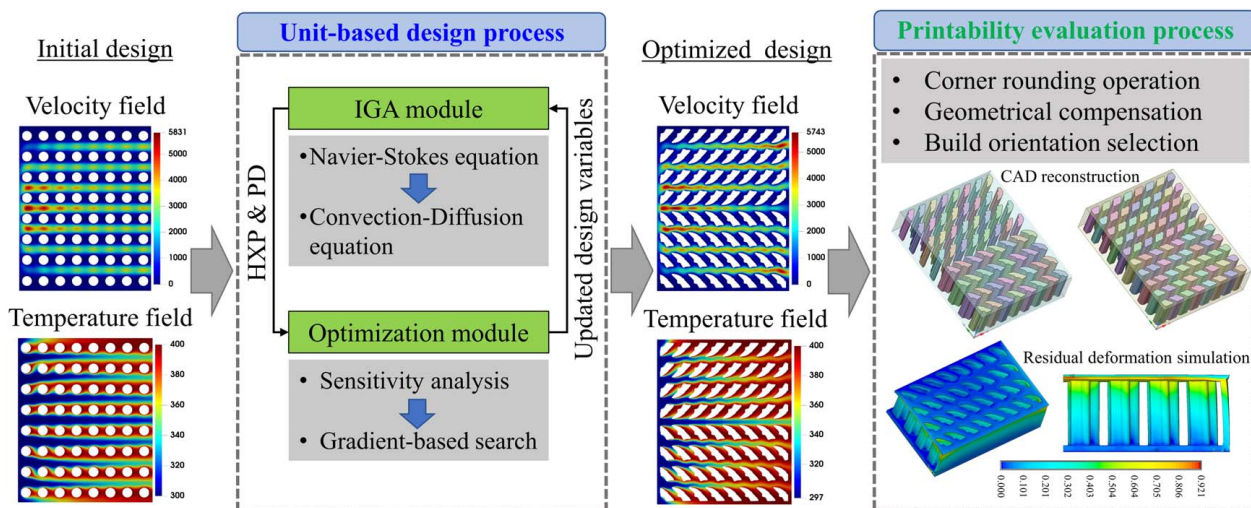


**Fig. 2** The framework overview for design and printability evaluation of the cross-flow HX with respect to the LPBF AM process. The IGA module is employed to evaluate the HXP and the PD, involved as the objective and constraint functions in the optimization module driven by the method of moving asymptotes. The optimized design is generated with a goal of the HXP maximization and meanwhile the PD control. 3D CAD reconstruction and residual deformation simulation are performed in the printability evaluation process. Some re-design work is proposed to improve printability of the optimized structures.



of the hot fluid in the channels is not considered regardless of the change of the channel shape in the design process. When the 3D problem is considered in the future, the out-of-plane hot flow will be modeled and its flow resistance will be considered in the optimization model.

To obtain the design variables, we define the configuration of the cross-flow HX through moving position and changing shape of the channels containing the hot fluid. The evolution of the hot fluid regions in the design domain is tracked by combining B-spline basis functions and a group of control points with an identical point as the beginning and ending control points. These components construct a closed curve to explicitly represent the interface between the cold and hot fluids. The enclosed voids denote the hot fluid regions accordingly. For a single void, assume that this void is divided into  $n$  angular segments. Accordingly,  $n+2$  control points ( $P_0, P_1, \dots, P_n, P_{n+1}$ , and  $P_0 = P_{n+1} = (P_1 + P_n)/2$ ) are needed to describe this void. Thus, the center position movement ( $x_c, y_c$ ) of the void/channel and radii of the control points ( $r_1, r_2, \dots, r_i, \dots, r_n$ ) are taken as the design variables for this optimization model. By adjusting the radii of the control points, the channel shape can be changed. By moving the center position and changing the shape, the voids may be merged or split. This explains how our design parameterization supports both shape and topology optimization.

We first divide the entire design domain into grid sub-domains. Second, shape/topology optimization based on a single channel, or unit, is performed. All the channels in the global configuration share the same set of design variables to update their positions and shape in the iterative optimization process. In other words, the re-designed configuration is distributed uniformly into the sub-domains; thus, characterizing the process as unit-based design for the cross-flow HX. This procedure greatly reduces the total number of design variables, in comparison to full-scale design, which allows variation of all channel configurations in the design domain. Moreover, the unit-based design can guarantee that the distance between two adjacent thin-walled channels is always smaller than the sub-domain size. By adjusting this distance, the vertically printed channels of the optimized design can be considered as inherent support structures for printing the overhang top cap encapsulating the cold fluid for the cross-flow HX.

As mentioned, the optimization model aimed at maximizing the HXP while controlling the PD for the cross-flow HX is presented as follows. Usually, a minimization form of the objective is used to formulate the implementation optimization model. We have

$$\begin{aligned} \min f(\Omega) &= -\text{HXP} \\ \text{s.t.} \quad \text{PD} &\leq \overline{\text{PD}} \\ x &\leq x_c, y_c \leq \bar{x}, r_i \leq r_i \leq \bar{r} \end{aligned} \quad (7)$$

where  $\Omega$  denotes the entire design domain, and  $\overline{\text{PD}}$  denotes the upper limit for the PD.  $x_c, y_c$ , and  $r_i$  represent the center position movements and the radii of the control points for the channels. These design variables are defined in a specific range with the lower ( $x, r$ ) and upper limit ( $\bar{x}, \bar{r}$ ) in the numerical examples.

The method of moving asymptotes (MMAs) [20] is employed to drive evolution of the channel configuration in the iterative optimization process. For this gradient-based optimization, sensitivity analysis is required. As a benefit of the unit-based design, the total number of design variables is small. Moreover, good efficiency of the IGA-based solver in solving the multiphysics governing equations has been shown in our previous work [21–23]. Therefore, as a straightforward choice, the finite difference method is adopted to solve derivatives of the objective and constraint functions with respect to the design variables.

## 4 Residual Deformation Simulation

In this section, the numerical simulation method is introduced to predict residual deformation of AM produced components based on

the MIS method. The extraction of accurate inherent strains for AlSi10Mg deposition for the LPBF process is presented first. The sequential analysis is then introduced for part-scale residual deformation modeling.

**4.1 Extraction of Inherent Strains.** As introduced in Ref. [14], a small-scale thermomechanical simulation is performed to capture typical residual strain evolution history. Only a small section containing two deposition layers is considered. The double ellipsoid heat source model [24] is employed to simulate the moving laser beam. In this small-scale point-wise process simulation, the practical AM process parameters are applied: laser power, laser scan velocity, and layer thickness. AlSi10Mg powder is chosen for printing the cross-flow HX in this paper attributing to its excellent heat conduction property. For the LPBF process, the laser power is 280 W, laser scan velocity is 0.95 m/s, and deposition layer thickness is 0.03 mm. Moreover, temperature-dependent material properties from the literature [25] are employed in the small-scale thermomechanical simulation. For material points in the two-layer model, residual strain evolution history is extracted at the end of the simulation. Based on the formulation for computing the inherent strains in the MIS method, the computed inherent strain vector is  $(-0.016, -0.016, 0.014)$  for AlSi10Mg. These three values represent normal inherent strain components. The first two components are in the layer-plane direction, while the third one is in the build direction, respectively. The inherent strains are considered as coefficients of thermal expansion when loaded onto large components in the part-scale simulation.

## 4.2 Modified Inherent Strain-Based Sequential Analysis.

The extracted inherent strains from Sec. 2 are loaded to the concerned part-scale model in a layer-by-layer fashion. To reduce the computational cost, 10–20 real printing layers can be lumped into a super layer with the equivalent thickness without sacrificing accuracy [5]. To simulate the real layer-wise AM process, layered materials of the part-scale model are deactivated in the beginning and sequentially activated from bottom to top. Note that tall metal component using this MIS-based simulation process would still be computationally very expensive despite the aid of super layers.

To validate the extracted inherent strains, residual deformation of a canonical part from the literature [25] is studied. In the MIS-based sequential analysis, 20 real printing layers (thickness 0.03 mm) are compiled into a super layer with the equivalent thickness of 0.6 mm. Accordingly, the numerical model contains 41 super layers. The AlSi10Mg material properties used are the elastic modulus of 76 GPa and yield strength of 314 MPa. Given geometrical symmetry, only a quarter section of the canonical part needs to be simulated, and symmetrical deformation constraints are applied. As observed in Fig. 3, the geometry is very complex since there is a cone-like structure with thin walls. Detailed information on part dimensions can be found in Ref. [25]. Eight-node brick element is adopted and the mesh for the quarter section is shown in Fig. 3 (left).

The predicted residual deformation profile is shown in Fig. 3 (right). Note that the simulation result for the quarter section is mapped onto the complete canonical part using symmetrical reflection in the postprocessing for better visualization. According to our simulation, the maximum normal shrinkage on the surface of the as-built canonical part is 0.22 mm, compared to the previously documented 0.25 mm [25]. In part, the difference is attributed to different methods for residual deformation simulation. Different from our MIS-based simulation, literature utilized a specific AM simulation software package for the canonical part. Despite the slight difference, the extracted inherent strains and the MIS-based sequential analysis have been validated for AlSi10Mg components fabricated by LPBF. Thus, we can rely on this MIS-based simulation tool to generate residual deformation prediction for thin-walled channel components.

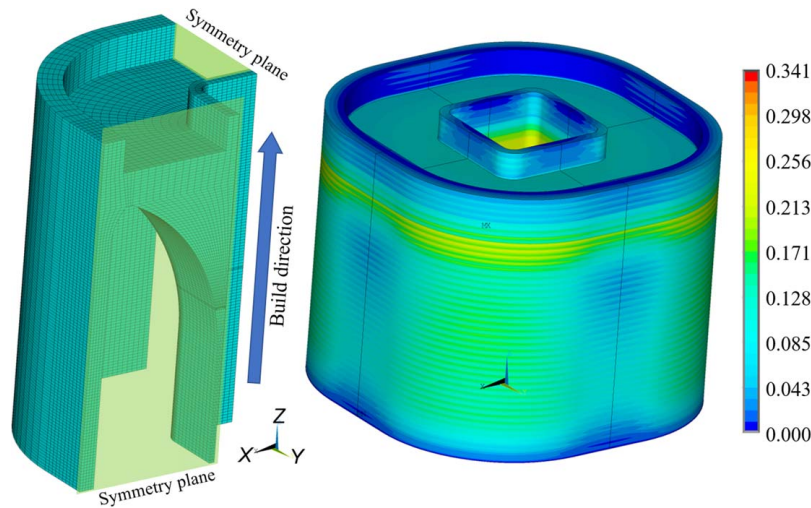


**Fig. 3 Mesh for a quarter section of the LPBF canonical part (left) and residual deformation profile obtained by the MIS-based simulation (right) using 41 super layers in the build direction**

## 5 Results and Discussions

The numerical results of some optimized 2D structures are first presented to demonstrate the effectiveness of the proposed unit-based design framework for the cross-flow HXs. Then, the printability of some optimized designs is evaluated based on the geometrical examination and residual deformation simulation, for which re-design work is performed to improve the printability with respect to the LPBF AM process. Lastly, some discussions are given based on our findings.

### 5.1 Unit-Based Design Examples

**5.1.1 Numerical Test Settings.** A rectangle of size  $0.08 \times 0.10 \text{ m}^2$  is employed as the design domain, typical printing dimension of a LPBF printer such as EOS M290. A  $200 \times 250$  uniform quad mesh is adopted as the control mesh. The fluid inlet velocity boundary condition adopts a parabolic distribution with a maximum value of  $40.0 \text{ m/s}$ . The dynamic viscosity  $\nu$  is set to  $0.01 \text{ N s/m}^2$ . The cold fluid inlet temperature is set to  $300 \text{ K}$ , and the temperature of hot fluid in the channels is set to  $400 \text{ K}$ . The thermal conductivity coefficient  $k_f$  is set to  $0.01 \text{ W/(m K)}$ . Regarding the design variables, 16 radius parameters are used to locate the control points and construct closed curves representing interface between the cold and hot fluids. For the gradient-based optimization process, when the iterative search reaches the prescribed maximum iteration number (e.g., 60), or when the difference of objective function values between two consecutive iterations is within the prescribed tolerance (e.g., 0.0001), the iteration process should be stopped.

In our implementation, the closed curves for hot regions are constructed using B-spline basis functions and refined by knot insertion. As a result, the closed curves are divided into 200 segments and approximated by polygons. The polygons in the lower half are mirrored to the upper half of the design domain. All the polygons in the global domain share the same set of design variables for shape update. The boundary conditions for fluid velocity and temperature fields are applied on the control points. An in-house code is employed to determine whether a control point is contained in the channels or not. For the control points inside the channels, zero velocity and a fixed high temperature are enforced as their boundary conditions. For the MMA-driven optimization process, a sensitivity study is needed. Herein, we computed the derivatives of the design variables with the forward difference method. Based on our trials, considering computational efficiency with the fewest iterations, we selected 0.001 (2.5 times of the mesh size) as the

step size in this section. Since 18 design variables (two center position movements and 16 radius parameters) are employed, 18 evaluations are needed to solve the derivatives in each optimization iteration.

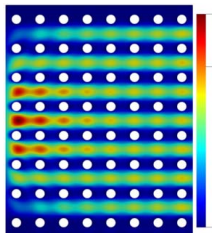
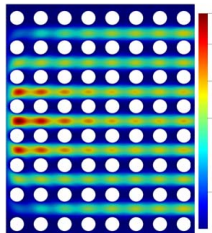
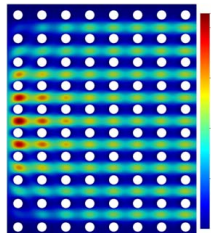
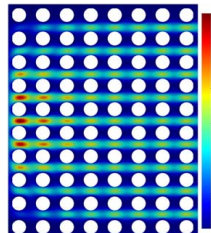
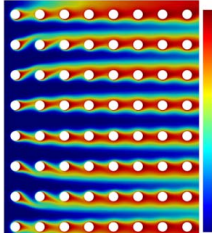
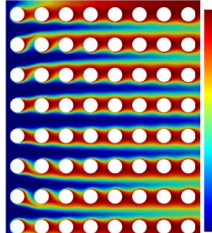
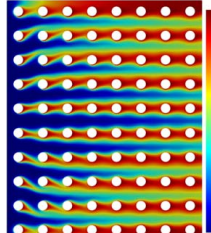
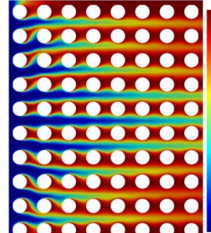
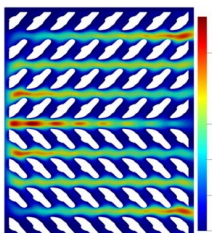
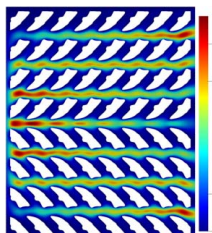
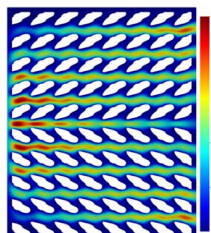
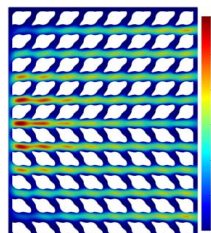
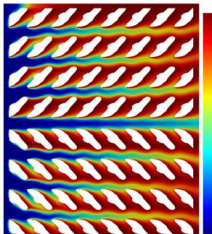
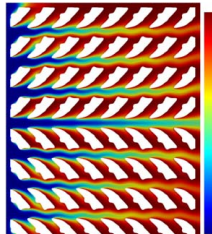
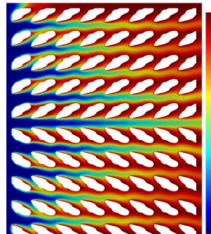
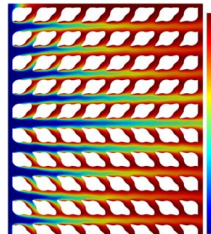
As observed in Fig. 1, when the cross-flow HX is printed vertically in the LPBF AM process, problems with structural integrity are encountered due to unsupported overhang of the top cap. When designing for LPBF AM, downward facing overhangs must be locally supported by bulk material because the underlying loose metal powder is unable to efficiently dissipate the heat from the previously melted layer. For the manufacturing of HXs, large local spacing between the channels can yield deformations in the printed design from lack of support. This problem is commonly encountered in domain-based design since sometimes the gap between channels is very large in the optimized structures. Thus, the unit-based design is proposed as a promising solution to regulate the spacing between channels in the effort to prevent deformation.

In addition, various powder bed-based printers have different tolerances for overhang feature dimensions. For example, the overhang tolerance is nearly  $0.005 \text{ m}$  for the EOS M290 printer. This explains why the canonical part can be fabricated successfully though a downward facing overhang feature is found in the connection region between the inner and outer walls. Given this fact, the rectangular design domain is divided into  $8 \times 8$  and  $8 \times 10$  units, respectively. In the proposed unit-based design, the channel configuration is optimized and distributed uniformly over the entire design domain. The configuration containing circular channels is employed as the initial design. The definition range of these design variables is set to  $[0.002, 0.01]$ . With consideration to the manufacturing limitation of gap size for EOS M290, a cutting gap of  $0.002 \text{ m}$  is adopted to guarantee that the channels avoid the design domain boundaries in the optimization process. The following numerical examples are performed on the Pittsburgh Supercomputing Center (PSC) Bridges-2 system [26] using 128 cores on one computing node.

**5.1.2 Unit-Based Design With Fixed Topology.** Four different initial designs are employed as shown in Table 1 in this example. Correspondingly, there are four different initial PD values in the unit of Pa. To obtain an improved HXP, it is reasonable to sacrifice the PD in the design process. We follow the study in Ref. [2] to select twice the initial PD value as the constraint. To set the same limit for all four cases, the initial PD values in the third and the last cases are averaged (nearly 5000), and 10,000 is selected as the upper limit (PD). The initial values of the radius design variables



**Table 1 Unit-based optimization results using different initial designs**

Number of units	8 × 8 radii = 0.002	8 × 8 radii = 0.003	8 × 10 radii = 0.002	8 × 10 radii = 0.003
$\ u\ ^2$ (initial)				
$T$ (initial)				
HXP (initial)	88.6	105.1	112.4	130.8
PD (initial)	2006	3878	3163	6902
$\ u\ ^2$ (optimized)				
$T$ (optimized)				
HXP (optimized)	143.9	146.8	159.1	158.6
Increase	62.4%	39.7%	41.5%	21.3%
PD (final)	7186	8742	7788	9933

are tested with 0.002 m and 0.003 m to study its influence on the optimization model. While only radii of the control points vary, the same topology and circular channel shapes are kept for the design domain in the initial designs.

Results of this preliminary analysis, shown in Table 1, demonstrate the dependence of the optimized results on the initial designs. This phenomenon suggests that the multiphysics topology optimization for the cross-flow HXs is a highly nonlinear problem, and different starting points yield distinct local optima by the gradient-based search. In general, the optimized channels have an airfoil-like shape, adjusting flow direction and velocity magnitude around the channels. As a result, heat transfer behavior between the hot and cold fluids is improved correspondingly. It is noted that the PD increases significantly during the optimization process, though the final PD values satisfy the prescribed constraint in all four cases. As a supplemental study, specifically for the cases in the second and the last columns in Table 1, the PD upper limit is set to 3878 and 6902, respectively, which is the same with its corresponding initial design in the second and the last columns. The initial designs in the first and the third columns are taken as the new initial designs, respectively, in the optimization process.

The optimization results are shown in Fig. 4. While the PD values are close, the new optimized structures have larger HXP than the initial designs in the second and the last columns in Table 1. This comparison demonstrates the HXP improvement of the cross-flow HXs using the proposed design framework.

Our study also demonstrates a trade-off between the HXP and the PD. Although more channels are contained in the initial design, the HXP of the design domain increases, while the PD increases significantly. When the same upper limit is used for the PD constraint, the HXP improvement for the optimized structure is not that large (e.g., ~21%, see the last column in Table 1) compared to the remaining cases. This is a limitation of the unit-based design. In this study, the topology of the design domain is fixed in the entire optimization process since the total number of channels is a constant. Due to many uniformly distributed channels, the PD value of the initial design can be very large, especially when the initial diameter of the channels is large. When a small upper limit is set for the PD, the initial PD may violate the constraint.

**5.1.3 Channel Shape Corner Rounding.** Some optimized structures may contain sharp corners caused by the optimization

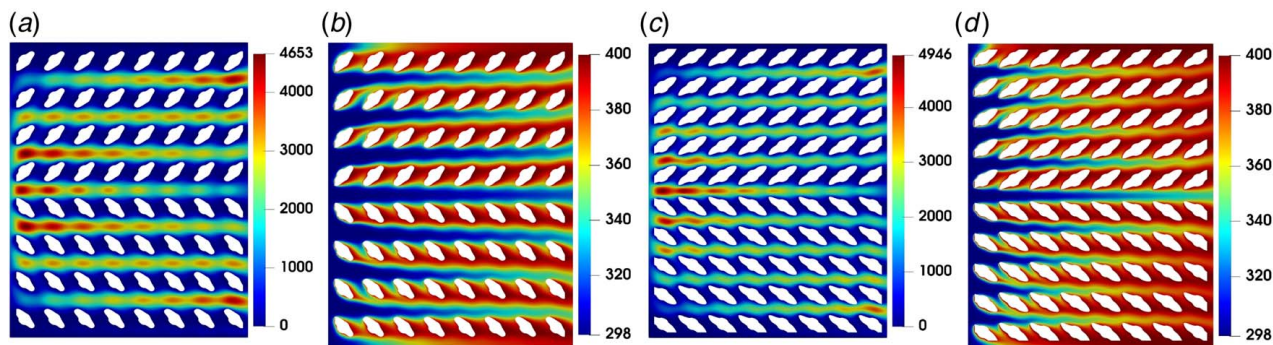


Fig. 4 The optimized structures using the upper limit of (a and b) 3878 and (c and d) 6902 as the PD constraint

itself and cutting given the boundary gap requirement (e.g., see the last column in Table 1). These sharp protrusions with acute angle are not suitable for the LPBF AM process as the heat buildup at these locations may lead to material accumulation. The excess material could collide with the moving roller for spreading powder layers, resulting in build failure and machine damage. Sharp features can also lead to unsupported overhangs from the top cap. This problem is attributed to the changing of the affected support range along the perimeter of the channel. To combat these problems related to sharp features, a corner rounding operation is employed to round off acute angles. The LPBF machine printing resolution, which is related to the laser beam size and metal powder size, induces some requirements the smoothed sharp corners should meet. For the original designs, the sharp corners with narrow angles cannot be captured due to the limitation of the printing resolution. Thus, we propose to use the rounding operation to eliminate sharp corners and ensure that the radius of the protruding feature is larger than the printing resolution.

Within this operation, a two-step approach is taken to mitigate the challenges that arise with sharp corners. The first step to increasing the angle degree of a sharp corner is by performing a simple operation for local expansion. Since each of the channels is a closed curve, the algorithm identifies the specific control point,  $r_i$ , and formulates a new radius using linear interpolation. For example, regarding the neighboring radius  $r_{i+1}$ , the new radius  $\hat{r}_{i+1}$  is generated by

$$\hat{r}_{i+1} = tr_i + (1 - t)r_{i+1} \quad (8)$$

where  $t$  takes a value from 0 to 1.

The second step explicitly addresses sharp corners caused by enforced cutting through filtering to remove these sharp features of the curve. Consider a new radius formed using  $t = 0.5$  with Eq. (8). By coupling these re-designed channels with the built-in Gaussian filtering tool in MATLAB, the processed structure can be reconstructed without any sharp corners, as shown in Fig. 6. This figure compares the unit-based design result from the last column of Table 1 with a structure which has undergone the proposed corner rounding operation. The processed configuration is more suitable for the bottom-up layer-wise printing process by the LPBF AM. However, due to the shape correction from the rounding operation, a slight change in the optimized HXP and PD values may occur with original unit-based design result. In particular, the HXP decreases to 154.9 and the PD increases to 10,205 for the corner-rounded structure as shown in Fig. 6(b). A slight violation is found for the PD constraint. To avoid this violation, it is suggested to manually tune the position of some channels to find a suitable configuration.

**5.1.4 Unit-Based Design With Evolving Topology.** In the following study, the channel in the single unit is allowed to move and split, rendering it accessible to distribute smaller number of circular channels in the initial design. Accordingly, the upper limit of the PD can be set to a smaller value without violation in the

beginning of our optimization. As a specific study, the design domain is divided into  $8 \times 4$  units. Two sets of design variables including the center position and the radii of control points are employed to describe the channels. In the first test, the same upper limit (10,000) is adopted for the PD constraint and the initial and optimized structures are shown in Fig. 5. Void splitting is observed, creating twice many channels compared with the initial design. The HXP value increases from 40.8 to 117.9, indicating an improvement of 189%. The PD increases from 735 to 6748, which is still below the prescribed upper limit.

In the second test, we set the upper limit of the PD to 3000 as an example. The same initial design is employed (see Figs. 5(a) and 5(b)). The optimized structure is shown in Figs. 5(e) and 5(f). In order to control the PD, the HXP improvement is sacrificed a little compared to the maximized HXP value in that case with a PD upper limit of 10,000. However, we still observe an increase of 173% from the initial to the optimized design, which is a very good improvement. Channel splitting is still observed. Due to a much smaller upper limit as the PD constraint, the average size of the channels in the optimized structure is smaller compared with the results in Figs. 5(c) and 5(d). An additional comparison is provided involving two fixed topologies containing  $8 \times 8$  and  $7 \times 6$  circular channels as shown in Figs. 5(g)–5(j). The radii of the circular channels are 0.0026 m and 0.004 m, respectively. The radius values are selected to ensure that the PD of the HX is nearly 3000. Based on the comparison, it shows that moving the position and changing the shape of the channels can help improve the HXP (from 98.3 to 111.4). Moreover, it indicates that distributing many small channels can improve the HXP (from 77.7 to 111.4) more effectively than employing fewer channels with a larger size.

In the third test, we divide the entire design domain into  $4 \times 4$  units and allow four groups of design variables, each of which contains two position variables for channel moving and 16 radius variables for channel deforming. The same initial design and the PD constraint with upper limit of 3000 are employed. The optimization results are shown in Figs. 5(k) and 5(l). A significant increase of 191% in the HXP is obtained, while the PD is well below the prescribed upper limit. The optimized HXP and PD values are better than results in the first and second tests. An explanation is that we have a higher chance to find a better optimum when more design variables are utilized. Channel splitting is also observed likely due to the proposed effort to distribute more channels for the improved HXP. Some channels disappear by moving out of the design domain, resulting in only two or three channels in the units. However, we find that the channels are not uniformly distributed and neighboring distance between some adjacent channels is very large. These designs are not suitable for practical LPBF AM process due to the previously mentioned overhang issue.

In comparison to the unit-based shape optimization for the fins in the cross-flow HXs in Ref. [27], a similar airfoil-like shape is found in the optimized structures of our numerical examples. It indicates that such channel shape is a reasonable selection indeed for improving the HXP of the HXs. Nonetheless, the density-based



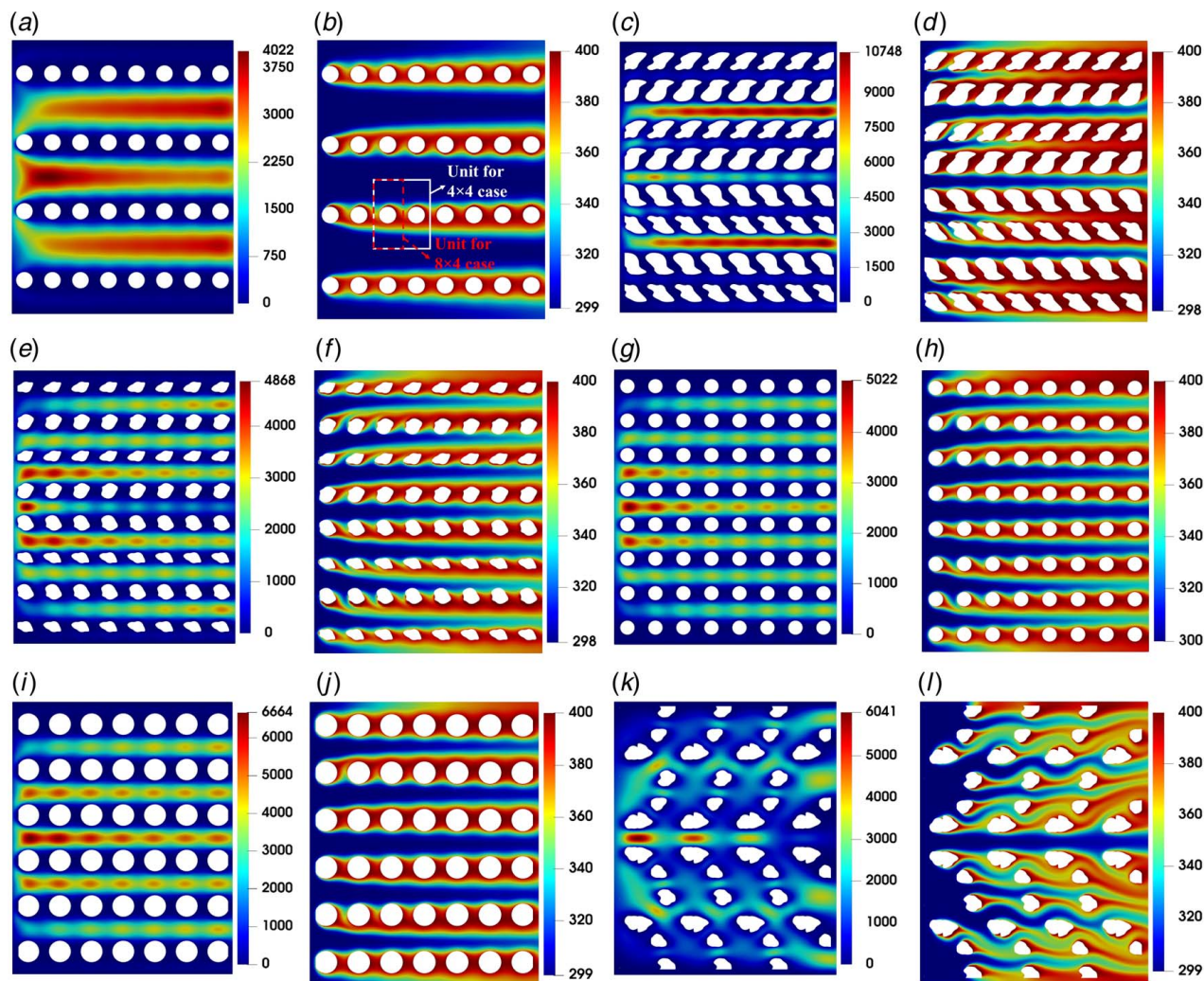


**Fig. 5** Initial design (a and b) and optimized structures (c–f, k, l) with the channels allowed to move and split during the optimization process. The unit domain is marked in (b). Upper limit of the PD is set to 10,000 for (c and d) and 3000 for (e, f, k, and l), respectively. Different splitting conditions are compared in (e and f) and (k and l). An additional comparison is provided in (g–j) using the fixed topologies containing  $8 \times 8$  and  $7 \times 6$  circular channels with the PD of nearly 3000.

optimization scheme in Ref. [27] results in zigzag boundary curves for the fins, while the proposed design framework can ensure smooth boundary curves for the channels in the optimization results, which is more suitable for the LPBF AM process. Moreover, the proposed unit-based design also supports topology optimization. Compared to the numerical examples based on the level-set-based shape and topology optimization for the cross-flow HXs in Ref. [2], the proposed design framework generates fewer sharp features, and always has explicit forms for the boundary curves of the optimized channels. This advantage provides the inherent convenience in converting the optimized structures into 3D files for AM use, which will be demonstrated in the following section.

**5.2 Re-design for Additive Manufacturing Printability Improvement.** The optimized structures are converted into 3D computer aided design (CAD) files through reconstruction for AM fabrication use. The 2D closed curves are extruded vertically into 3D thin-walled channels. In this paper, the thin-walled channels have a fixed wall thickness of 0.5 mm and a height of 20 mm. By setting the thickness of the surrounding walls to 2 mm, the entire build dimensions of the 3D cross-flow HX are  $80 \times 104 \times 24 \text{ mm}^3$ , accordingly. Once in 3D form, the structures may need additional reconstruction for manufacturing by LPBF using the

laser process parameters mentioned in Sec. 4. The island scanning strategy is recommended for printing the unit-based design results. With these defined processing parameters, we propose three re-design strategies in this section: shape corner rounding operation, geometrical compensation, and build orientation selection. All the re-design operations are implemented after the optimized designs are obtained.

**5.2.1 Geometrical Compensation.** When the 3D cross-flow HX is printed by the LPBF AM process, geometrical inaccuracy is encountered due to residual deformation. We use numerical simulation to predict residual deformation, and then implement geometrical compensation to reduce geometrical inaccuracy of the final build. The super layer thickness is set to 0.5 mm. As a result, we need 48 super layers for the 24 mm high HX in the MIS-based sequential analysis to compute final residual deformation.

The optimized structures in the second ( $8 \times 8$  case) and the last columns ( $8 \times 10$  case) of Table 1 are taken as examples. Corner rounding has been applied to all the channels before performing residual deformation simulation. Due to symmetry of the structure, we only need to simulate half of the entire cross-flow HX through the MIS-based layer-wise analysis. Hexahedral elements are adopted to mesh the half model, and the mesh for the  $8 \times 8$  case is shown in Fig. 7 as an example. The average side length of the



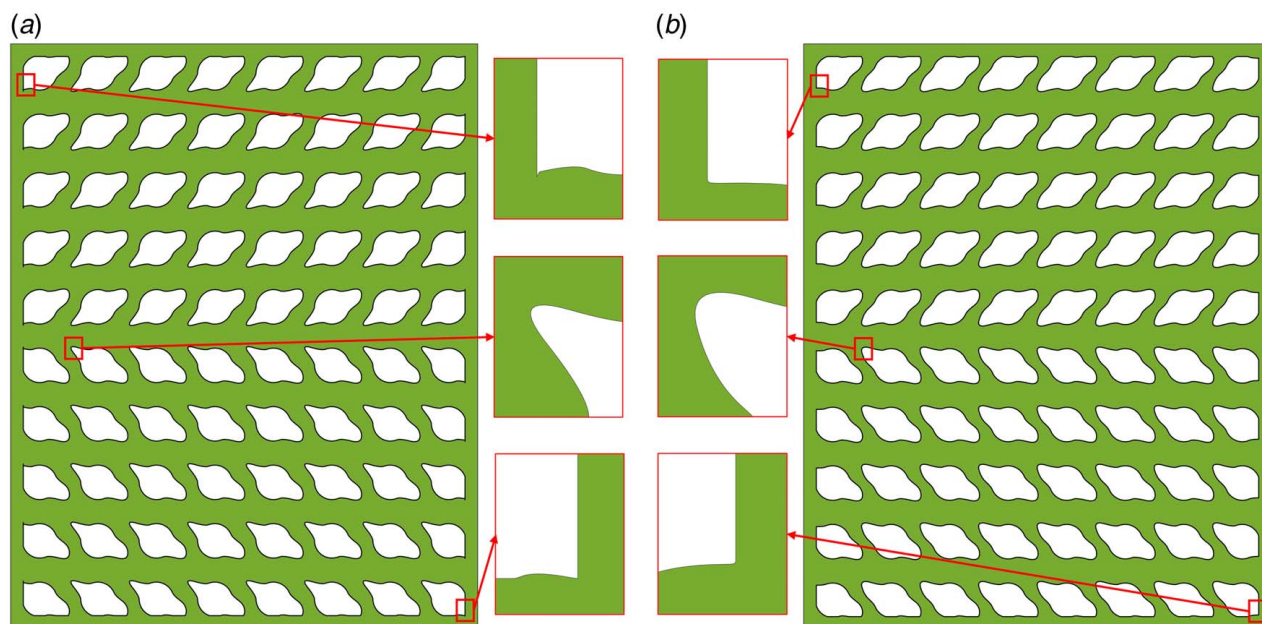


**Fig. 6 Comparison between the (a) raw and (b) processed structure from the unit-based design. Sharp corners in (a) are removed by the rounding operation in (b), making the re-designed structure more friendly to the LPBF process.**

elements is 0.5 mm, and the total number of elements is 205,773 and 205,664 for the corner-rounded optimized design in the  $8 \times 8$  and  $8 \times 10$  cases, respectively. Due to the large number of elements and many load steps, it takes nearly 2.2 h to finish the sequential analysis. Additionally, the initial design containing  $8 \times 8$  circular channels is also simulated as a comparison, taking 2.6 h with 206,336 elements.

The predicted residual deformation profiles of the as-built cross-flow HX are shown in Fig. 7. The dominant shrinkage occurs at the interface between the top cap and the vertical thin-walled channels (see the circles in Figs. 7(d) and 7(e)). Especially, the normal shrinkage of the initial design is much larger than the optimized design. In other words, the initial design is not printable in practice. This phenomenon is caused by discontinuity of cross section in the build direction, which has also been reported in other literatures [25,28]. Given the configuration of cross-flow HX, this issue is inherent. However, geometrical compensation can be employed to reduce geometrical inaccuracy in the final build [15,29]. The basic idea of compensation is to reverse the direction of residual deformation and add this variation to the original geometry correspondingly. For example, the compensated side walls in these two cases are shown in Fig. 8. The optimized structure after geometrical compensation is converted into a CAD file and used for practical printing. In this way, the as-built build after AM production is expected to have a geometrical dimension close to the targeted component. In addition, according to our experience, after cutting from the build substrate, bending-up residual deformation becomes significant due to the release of residual stress in the deposition–substrate interface. Adopting designed support structure below the HX build could be a promising solution to mitigating the after cutting residual deformation, which will be studied in the future.

**5.2.2 Build Orientation Selection.** Although the unit-based design result satisfies the small PD upper limit, as shown in Figs. 5(e) and 5(f), additional support is needed underneath the top cap as distance between the channels is larger than the maximum overhang feature limitation of the EOS M290 printer. A direct solution is to insert additional thin walls like the side walls between the channels as support structures for the top cap. However, the fabrication process would consume more metal

powders to deposit the support structures. Moreover, it is very difficult to remove the support structures in the postprocessing since the internal configuration of the 3D cross-flow HX is very complex.

To address the above concern, build orientation of the cross-flow HX can be re-designed to enhance its printability [15]. For this study, we will characterize build orientation based on the incline angle, the angle between the bottom cap and substrate plane. Generally, the critical incline angle for the LPBF AM process is 45 deg, regardless of different metal powders [30,31]. Printing success can be guaranteed for solid components with regular geometry when the build angle is not smaller than 45-deg. However, for a component with complex internal configuration, it is often very challenging to find an incline angle that can avoid overhang issue for all local features. With respect to the cross-flow HX, since the top cap and thin-walled channels are perpendicular, the 3D CAD file of the cross-flow HX can only be inclined by an angle of 45-deg to avoid potential overhang issue. Nonetheless, due to the sharp corner between the bottom cap and side walls, a specific base must be added to provide a strong connection between the build and the substrate. The re-designed configuration of the cross-flow HX is shown in Fig. 9.

Consequently, there are a few trade-offs when applying this re-design approach. One is that metal powder consumption and print time will be increased by either adjusting the incline angle or inserting support structures. This is most apparent when larger incline angles are adopted for a printable component yielding an increase in effective build height, resulting in more layering. Moreover, due to change of build orientation, residual deformation pattern would be quite different from the HX printed in the vertical direction. As a trade-off, slice of the side walls forms sharp protrusions against the metal roller spreading powders, which may cause build failure. Therefore, a brush roller is suggested for printing the inclining HX.

**5.3 Discussions.** In general, unit-based design is able to improve the HXP, control the PD, and meanwhile provide optimized configuration with moderate printability for the cross-flow HX. Both shape and topology optimization are allowed in the developed unit-based design framework. We find that arranging more channels is helpful to improve the HXP and AM printability since vertical channels are inherent support structures for the top

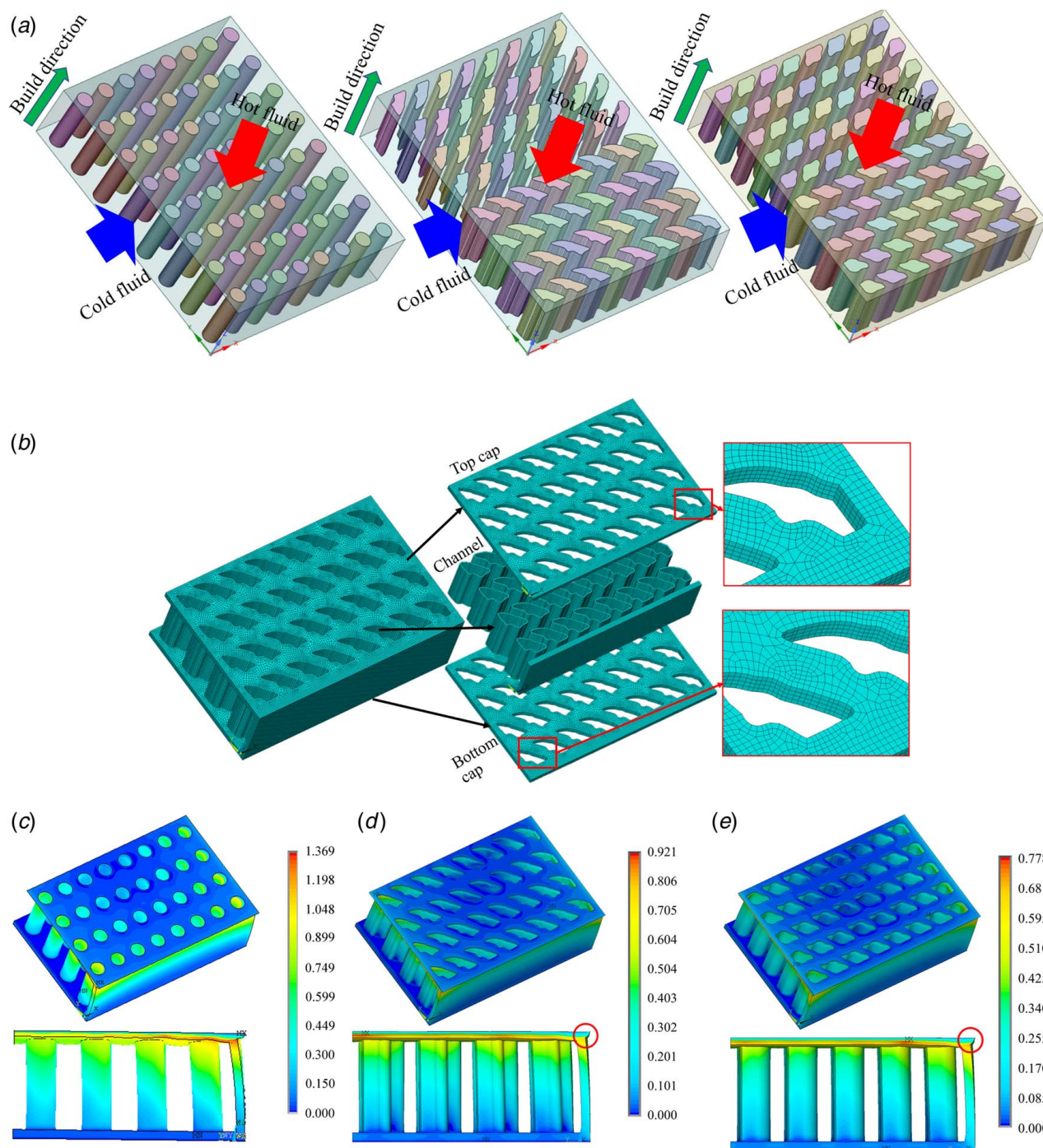


**Fig. 7 MIS-based analysis for residual deformation prediction. (a) The 3D HX model contains top, bottom caps, side walls, and vertical channels. (b) Hexahedral elements are adopted in the mesh. (c–e) Residual deformation profiles for initial and optimized structures are plotted in different views with unit of mm.**

cap, but may increase the PD significantly. If the PD control is of priority, we have to sacrifice printability of the optimized structure, such as allowing overhang issue caused by sparse and small channels.

Unit-based design results, however, are not entirely friendly to the LPBF AM process due to unwanted features like sharp corners and overhang issue. Therefore, re-design work is needed to improve practical printability of the conceptual design. The corner rounding operation is the basic procedure. Unwanted geometrical features such as sharp protrusions and steep corners of the thin-walled channels should be eliminated. Before entering a practical AM process, the numerical simulation should be

performed to compute residual deformation of the as-built HX. If overlarge residual deformation is observed, geometrical compensation should be carried out to improve geometrical accuracy of the final build. Whereas, this simulation process would be computationally very expensive if build height of the cross-flow HX is very large. In addition, build orientation selection can be an alternative solution to handle the overhang issue in some unit-based design results. However, changing build orientation of the cross-flow HX may cause new risk of build failure. Employing support structures for the inclining HX is a promising operation that enhances connection between the build and the substrate so that build failure could be avoided.



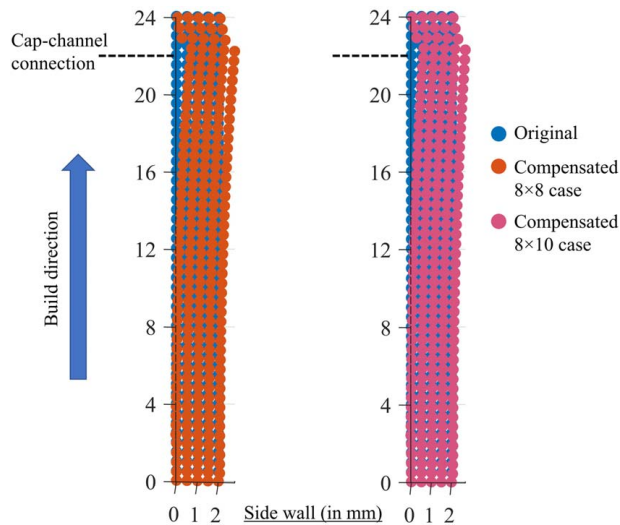


**Fig. 8 Compensated side walls based on residual deformation simulation. Residual deformation is reversed in direction and added to the original geometry.**

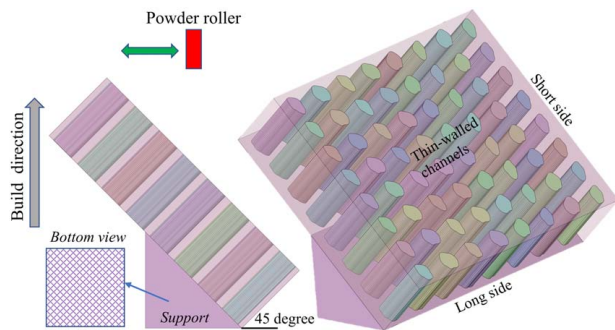


**Fig. 9 Re-designed HX with the build orientation of 45 deg. Support structures are required to provide strong connection between the build and substrate. Long side is laid on the build plate to reduce effective build height.**

## 6 Conclusions and Future Work

In this paper, the design and printability evaluation of the cross-flow HX is studied considering specific requirement for the LPBF AM technology. A workflow is established, consisting of the unit-based design and printability evaluation processes. In the unit-based design process, IGA is employed to solve 2D multiphysics equations for fluid velocity, pressure, and temperature fields, and compute the HXP and the PD for the cross-flow HX. The entire design domain is divided into many units/sub-domains, enforcing existence of channels given the concern on practical AM printability. Gradient-based optimization is employed to drive evolution of the channel configuration for the purpose of maximizing the HXP and controlling the PD. We observe that the optimization results highly depend on initial designs, indicating strong nonlinearity of the multiphysics optimization problem for the HXs. We find that the design process tends to distribute many channels to improve the HXP, while increasing the PD significantly. When a tight PD constraint with small upper limit is enforced, the optimization result still prefers to have many channels but with large distance in between, resulting in overhang issue for top cap when the cross-flow HX is printed vertically by the LPBF process.

In the printability evaluation process, optimized structural configuration is carefully examined to ensure good manufacturability. The shape corner rounding operation is implemented as a very first step.

By adjusting local radius and filtering curve points, we successfully remove sharp protrusions and steep corners of the channels, making the re-designed configuration more friendly to the layer-wise printing process. Following that, residual deformation simulation is performed and significant shrinkage is observed. Geometrical compensation is proposed to improve geometrical accuracy of the final build of cross-flow HX. Finally, for some unit-based design results with overhang issue, build orientation selection is studied, and a 45-deg orientation is suggested specifically for printing the cross-flow HX. The proposed workflow enables interaction between upstream design stage and downstream AM fabrication stage. Therefore, it has huge potential in application to industrial fields.

In the future, support structure design through topology optimization will be studied to mitigate residual deformation of the printed HX. Additionally, experimental study will be performed to validate the AM printability of our design results, evaluate the real HXP, and measure the PD of the printed designs.

## Acknowledgment

Research was sponsored by the Army Research Laboratory and was accomplished under Cooperative Agreement Number W911NF-18-2-0162. The views and conclusions contained in this document are those of the authors and should not be interpreted as representing the official policies, either expressed or implied, of the Army Research Laboratory or the U.S. Government. The U.S. Government is authorized to reproduce and distribute reprints for Government purposes notwithstanding any copyright notation herein. This work used the Extreme Science and Engineering Discovery Environment (XSEDE), which is supported by National Science Foundation Grant No. ACI-1548562. Specifically, it used the Bridges-2 system, which is supported by NSF award number ACI-1928147, at the PSC.

## Conflict of Interest

There are no conflicts of interest.

## Data Availability Statement

The datasets generated and supporting the findings of this article are obtainable from the corresponding author upon reasonable request.

## Nomenclature

$p$	= fluid pressure field
$\mathbf{u}$	= fluid velocity field
$T$	= fluid temperature field
$\mathbf{E}$	= constitutive elasticity tensor
$\mathbf{F}$	= body force
$c_p$	= thermal capacity coefficient of the fluid
$k_f$	= thermal conductivity coefficient of the fluid
$\mathbf{u}_0$	= fluid inlet velocity
Pe	= Peclet number
Re	= Reynolds number
$\varepsilon$	= strain field of metal build
$\nu$	= dynamic viscosity of the fluid
$\rho$	= mass density of the fluid
$\sigma$	= stress field of metal build

## References

- [1] Dbouk, T., 2017, "A Review About the Engineering Design of Optimal Heat Transfer Systems Using Topology Optimization," *Appl. Therm. Eng.*, **112**, pp. 841–854.

- [2] Feppon, F., Allaire, G., Dapogny, C., and Jolivet, P., 2021, "Body-Fitted Topology Optimization of 2D and 3D Fluid-to-Fluid Heat Exchangers," *Comput. Methods Appl. Mech. Eng.*, **376**, p. 113638.
- [3] Mohammadi, M., Abbasi, H., Yavarinasab, A., and Pourrahmani, H., 2020, "Thermal Optimization of Shell and Tube Heat Exchanger Using Porous Baffles," *Appl. Therm. Eng.*, **170**, p. 115005.
- [4] Moon, H., McGregor, D., Miljkovic, N., and King, W., 2021, "Ultra-Power-Dense Heat Exchanger Development Through Genetic Algorithm Design and Additive Manufacturing," *Joule*, **5**(11), pp. 3045–3056.
- [5] Liang, X., Chen, Q., Cheng, L., Hayduke, D., and To, A., 2019, "Modified Inherent Strain Method for Efficient Prediction of Residual Deformation in Direct Metal Laser Sintered Components," *Comput. Mech.*, **64**(6), pp. 1719–1733.
- [6] Tran, H., Chen, Q., Mohan, J., and To, A., 2020, "A New Method for Predicting Cracking at the Interface Between Solid and Lattice Support During Laser Powder Bed Fusion Additive Manufacturing," *Addit. Manuf.*, **32**, p. 101050.
- [7] Liu, J., Gaynor, A., Chen, S., Kang, Z., Suresh, K., Takezawa, A., Li, L., Kato, J., Tang, J., Wang, C. C., Cheng, L., Liang, X., and To, A. C., 2018, "Current and Future Trends in Topology Optimization for Additive Manufacturing," *Struct. Multidiscipl. Optim.*, **57**(6), pp. 2457–2483.
- [8] Rosen, D., 2014, "Design for Additive Manufacturing: Past, Present, and Future Directions," *ASME J. Mech. Des.*, **136**(9), p. 090301.
- [9] Kubalak, J., Wicks, A., and Williams, C., 2021, "Investigation of Parameter Spaces for Topology Optimization With Three-Dimensional Orientation Fields for Multi-Axis Additive Manufacturing," *ASME J. Mech. Des.*, **143**(5), p. 051701.
- [10] Mezzadri, F., Bouriakov, V., and Qian, X., 2018, "Topology Optimization of Self-Supporting Support Structures for Additive Manufacturing," *Addit. Manuf.*, **21**, pp. 666–682.
- [11] Liang, X., To, A., Du, J., and Zhang, Y., 2021, "Topology Optimization of Phononic-Like Structures Using Experimental Material Interpolation Model for Additive Manufactured Lattice Infills," *Comput. Methods Appl. Mech. Eng.*, **377**, p. 113717.
- [12] Takezawa, A., To, A., Chen, Q., Liang, X., Dugast, F., Zhang, X., and Kitamura, M., 2020, "Sensitivity Analysis and Lattice Density Optimization for Sequential Inherent Strain Method Used in Additive Manufacturing Process," *Comput. Methods Appl. Mech. Eng.*, **370**, p. 113231.
- [13] Liang, X., Cheng, L., Chen, Q., Yang, Q., and To, A., 2018, "A Modified Method for Estimating Inherent Strains From Detailed Process Simulation for Fast Residual Distortion Prediction of Single-Walled Structures Fabricated by Directed Energy Deposition," *Addit. Manuf.*, **23**, pp. 471–486.
- [14] Chen, Q., Liang, X., Hayduke, D., Liu, J., Cheng, L., Oskin, J., Whitmore, R., and To, A., 2019, "An Inherent Strain Based Multiscale Modeling Framework for Simulating Part-Scale Residual Deformation for Direct Metal Laser Sintering," *Addit. Manuf.*, **28**, pp. 406–418.
- [15] Chowdhury, S., Mhapsekar, K., and Anand, S., 2018, "Part Build Orientation Optimization and Neural Network-Based Geometry Compensation for Additive Manufacturing Process," *ASME J. Manuf. Sci. Eng.*, **140**(3), p. 031009.
- [16] Chahal, V., and Taylor, R. M., 2020, "A Review of Geometric Sensitivities in Laser Metal 3D Printing," *Virtual Phys. Prototyp.*, **15**(2), pp. 227–241.
- [17] Hughes, T., Cottrell, J., and Bazilevs, Y., 2005, "Isogeometric Analysis: CAD, Finite Elements, NURBS, Exact Geometry and Mesh Refinement," *Comput. Methods Appl. Mech. Eng.*, **194**(39), pp. 4135–4195.
- [18] Bazilevs, Y., Calo, V., Hughes, T., and Zhang, Y., 2008, "Isogeometric Fluid-Structure Interaction: Theory, Algorithms, and Computations," *Comput. Mech.*, **43**(1), pp. 3–37.
- [19] Casquero, H., Wei, X., Toshniwal, D., Li, A., Hughes, T., Kiendl, J., and Zhang, Y., 2020, "Seamless Integration of Design and Kirchhoff-Love Shell Analysis Using Analysis-Suitable Unstructured T-Splines," *Comput. Methods Appl. Mech. Eng.*, **360**, p. 112765.
- [20] Svanberg, K., 1987, "The Method of Moving Asymptotes—A New Method for Structural Optimization," *Int. J. Numer. Methods Eng.*, **24**(2), pp. 359–373.
- [21] Liang, X., Li, A., Rollett, A., and Zhang, Y., 2022, "An Isogeometric Analysis Based Topology Optimization Framework for 2D Cross-Flow Heat Exchangers With Manufacturability Constraints," *Eng. Comput.*, pp. 1–24.
- [22] Casquero, H., Zhang, Y., Bona-Casas, C., Dalcin, L., and Gomez, H., 2018, "Non-Body-Fitted Fluid-Structure Interaction: Divergence-Conforming B-Splines, Fully-Implicit Dynamics, and Variational Formulation," *J. Comput. Phys.*, **374**, pp. 625–653.
- [23] Li, A., Chai, X., Yang, G., and Jessica Zhang, Y., 2019, "An Isogeometric Analysis Computational Platform for Material Transport Simulations in Complex Neurite Networks," *Mol. Cell. Biomech.*, **16**(2), pp. 123–140.
- [24] Goldak, J., Chakravarti, A., and Bibby, M., 1984, "A New Finite Element Model for Welding Heat Sources," *Metall. Trans. B*, **15**(2), pp. 299–305.
- [25] Soylemez, E., Koc, E., and Coskun, M., 2019, "Thermo-mechanical Simulations of Selective Laser Melting for AlSi10Mg Alloy to Predict the Part-Scale Deformations," *Prog. Addit. Manuf.*, **4**(4), pp. 465–478.
- [26] Towns, J., Cockerill, T., Dahan, M., Foster, I., Gauthier, K., Grimshaw, A., Hazlewood, V., Lathrop, S., Lifka, D., Peterson, G. D., and Roskies, R., 2014, "XSEDE: Accelerating Scientific Discovery," *Comput. Sci. Eng.*, **16**(5), pp. 62–74.
- [27] Mekki, B. S., Langer, J., and Lynch, S., 2021, "Genetic Algorithm Based Topology Optimization of Heat Exchanger Fins Used in Aerospace Applications," *Int. J. Heat Mass Transfer*, **170**, p. 121002.
- [28] Liang, X., Dong, W., Chen, Q., and To, A., 2021, "On Incorporating Scanning Strategy Effects Into the Modified Inherent Strain Modeling Framework for Laser Powder Bed Fusion," *Addit. Manuf.*, **37**, p. 101648.
- [29] Nguyen, L., Buhl, J., Israr, R., and Bambach, M., 2021, "Analysis and Compensation of Shrinkage and Distortion in Wire-Arc Additive Manufacturing of Thin-Walled Curved Hollow Sections," *Addit. Manuf.*, **47**, p. 102365.
- [30] Shange, M., Yadroitsava, I., du Plessis, A., and Yadroitsev, I., 2022, "Roughness and Near-Surface Porosity of Unsupported Overhangs Produced by High-Speed Laser Powder Bed Fusion," *3D Print. Addit. Manuf.*, **9**(4), pp. 288–300.
- [31] Wu, Z., Narra, S., and Rollett, A., 2020, "Exploring the Fabrication Limits of Thin-Wall Structures in a Laser Powder Bed Fusion Process," *Int. J. Adv. Manuf. Technol.*, **110**(1), pp. 191–207.